

## **The Development of TiNi-based Negative Poisson's Ratio Structure using Selective Laser Melting**

*Sheng Li<sup>1</sup>, Hany Hassanin<sup>2</sup>, Moataz Attallah<sup>1\*</sup>, Nicholas Adkins<sup>1</sup>, and Khamis Essa<sup>3</sup>*

<sup>1</sup>*School of Metallurgy and Materials, University of Birmingham, Edgbaston, Birmingham, B15 2TT, UK*

<sup>2</sup>*School of Mechanical and Automotive Engineering, Kingston University, London, SW15 3DW*

<sup>3</sup>*School of Mechanical Engineering, University of Birmingham, Edgbaston, Birmingham, B15 2TT, UK22S3*

**Keywords:** Shape Memory alloys, Selective Laser Melting, Microstructural Development, Heat Treatment, Negative Poisson's Ratio Structures

### **Abstract**

There is a growing interest in using additive manufacturing to produce smart structures, which have the capability to respond to thermal and mechanical stimuli. In this report, Selective Laser Melting (SLM) is used to build a Negative Poisson's Ratio (NPR) TiNi-based Shape Memory Alloy (SMA) structure, creating a multi-functional structure that could be used as reusable armour. The study assesses the influence of SLM process parameters (laser power, scan speed, and track spacing) on the microstructural and structural integrity development in a Ti-rich TiNi alloy, as well as the impact of the post-process homogenisation treatment on the microstructure and phase transformations. The builds generally shows stress-induced cracks and residual porosity, which could be minimised through process optimisation. Nonetheless, the homogenisation treatment is essential to reduce the fraction of Ti<sub>2</sub>Ni intermetallics, which are known to disturb the B19'-chemistry, and hence the required phase transformation temperatures. The optimum process parameters are finally used to fabricate NPR structures, which were mechanically tested to validate the Poisson's ratio predictions. A higher ductility was observed in the structures that have undergone the homogenisation treatment.

## 1. Introduction

Negative Poisson's Ratio (NPR) structures, also known as auxetics, are interconnected network-like structures which grow in size when stretched or shrink when compressed <sup>[1]</sup>. This unique property offers an enhanced functionality in the mechanical performance of these structures. Compared to conventional structures, NPR structures offer an increased plane strain, and a tuneable density, fracture resistance, shear modulus, indentation resistance and acoustic response <sup>[2]</sup>. Accordingly, NPR structures have been considered for a wide range of smart and functional devices, including smart antennas <sup>[3]</sup>, stretchable sensors <sup>[4]</sup>, protective equipment <sup>[5]</sup> and in many other applications from the fields of nanotechnology and biomedicine to defence and aerospace. Despite these advantages, the complex designs of NPR structures pose difficulties in manufacturing, and hence limit their applications. To date, many reports on NPR structure are focused on the theoretical analysis and the material response. Different types of NPR structures have been developed. This includes cellular solids <sup>[6-11]</sup>, porous polymers <sup>[12-14]</sup>, composites <sup>[15-17]</sup>, and textiles <sup>[18-19]</sup>.

Conventional sheet forming processes have been employed to construct cellular NPR structures <sup>[20]</sup>. However, the size and design limitations are considered to be the main barrier to produce complex NPR structure. Electron Beam Melting (EBM), one of the additive manufacturing (AM) processes, has been also used to fabricate 3D re-entrant NPR structure made from Ti-6Al-4V <sup>[21]</sup>.

NPR structures have been categorised into several types such as 'chiral', re-entrant 'and 'rotating', honeycomb, and others. Elip et al. conducted a comparative study of 2D and 3D NPR geometries using simulation and CAD/CAE. They found that the re-entrant 2D and 3D geometries have the highest negative Poisson's ratio and the lowest area reduction. On the other hand, the 2D chiral and 3D pyramid NPR structures proved to have the highest area reduction and the lowest negative Poisson's ratio <sup>[22]</sup>.

To enhance the functionality of NPR structures, TiNi-based Shape Memory Alloys can be used, combining this with the use of AM to utilise the design flexibility it offers. TiNi-based SMAs are known to exhibit a motor-functionality due to a reversible phase transformation <sup>[23]</sup>. The phase transformation (e.g. B19' martensite  $\leftrightarrow$  B2 austenite) can either be deformation-induced or temperature-induced, which is referred to as superelasticity (SE) or the shape memory effect (SME), respectively, depending on the alloy chemistry and the phases present <sup>[24]</sup>. This metallurgical behaviour makes SMAs a candidate class for shock-absorbing, inflatable, or actuating structures, as they can recover their original shape following deformation, with or without a thermal stimulus. Nonetheless, manufacturing of SMAs via conventional manufacturing (e.g. ingot casting and hot deformation) is known to result in various defects due to their high susceptibility to cracking and segregation <sup>[25, 26]</sup>, in addition to their poor machinability <sup>[27, 28]</sup>. Furthermore, the phase transformations, and hence the SMAs performance, are highly sensitive to the alloy chemistry (e.g. Oxygen and Carbon content) <sup>[29, 30]</sup>, resulting in an irreproducible and variable behaviour. As such, there is an interest in exploring novel manufacturing processes that could avoid these concerns, while improving the geometrical complexity of SMAs structures. The use of AM technologies is a potential route that may address the aforementioned issues, due to its design flexibility, as well as the localised heating and rapid cooling rates associated with the process, which may reduce the extent of segregation and the grain size, resulting in structures with improved mechanical performance compared to casting.

Selective Laser Melting (SLM), or laser powder bed fusion, is an AM technology that uses powders melted layer-by-layer to create complex 3D structures <sup>[31]</sup>. The geometrical and surface accuracy of SLM process is typically better than those in the EBM <sup>[32]</sup>, and therefore was chosen for this work. Previous work on SLM processing of TiNi followed three approaches; the first involved the use of mixed elemental Ni and Ti powders <sup>[33]</sup>, while the second approach focused on SLM processing of porous structures with controlled porosity for

bone implants to achieve the bone's specific strength and modulus (i.e. biomechanical compatibility) <sup>[34, 35]</sup>, and the third starting from pre-alloyed powders to create dense structures <sup>[36-38]</sup>. For a comprehensive review on AM of TiNi, the reader is directed to the review by Elahinia *et al.* <sup>[39]</sup>. Nonetheless, studies on AM of TiNi have suffered from a number of shortcomings. First, the majority of the studies focused on Ni-rich or equi-atomic TiNi <sup>[40, 41]</sup>, where SE is the dominant SMA regime, understandably since the majority of SMA applications in the medical field (e.g. stents) rely on the SE behaviour rather than the SME. In contrast, Ti-rich TiNi applications (e.g. actuators) rely on the SME in achieving the motor-functionality, and they demonstrate a higher strength due to precipitation strengthening via Ti<sub>2</sub>Ni <sup>[42, 43]</sup>. Furthermore, the transformation temperatures (TTs) in Ti-rich TiNi are less sensitive to the Ni-content. Nonetheless, Ti-rich are specifically susceptible to liquid (weld) cracking due to grain boundary segregation <sup>[39, 42]</sup>. Second, the previous studies overlooked the need for post-processing homogenisation treatments to reduce segregation. Homogenisation of TiNi is known to result in a reproducible behaviour, with less variation in the TTs <sup>[43]</sup>. Finally, the utilisation of SLM design flexibility in developing and assessing the behaviour of multi-functional TiNi structures (e.g. negative Poisson's ratio auxetic structures) is fairly limited <sup>[44, 45]</sup>. These shortcomings, and others, are addressed in the present investigation.

The aim of this work is to introduce a novel type of a smart metamaterial that combines the properties of both NPR structures and SMAs in one component, and is manufactured using AM. This combination may hold the potential to create multifunctional auxetic structures, for instance to produce a reusable adaptive armour. The main objectives were to design, model, fabricate, and to mechanically test TiNi SMA NPR re-entrant structures, fabricated using SLM, to establish design-process-microstructure-mechanical performance correlations, through the application of Finite Element Analysis (FEA), process optimisation, and advanced materials characterisation.

## **2. Experimental**

### **2.1. Material and SLM Processing**

A Ti<sub>56</sub>Ni<sub>44</sub> (55.7 at.% Ti content) cast, homogenised, and forged ingot was argon atomised by TLS Technik GmbH&Co (Germany). The powder was later sieved to separate the <65 µm which was used for SLM processing. The O-content of the as-received powder was measured using Leco TC436AR ANALYSER, and was found to be 1000 ppm. The particle size distribution of the powder was measured using a CoulterLS230 laser diffraction particle size analyser.

Samples of dimensions (*x,y,z*) of 5×5×10 mm<sup>3</sup> were built using a Concept Laser M2 Cusing SLM (laser powder bed) system in an Ar atmosphere, with an oxygen-content <0.1%. The system uses a continuous wave fibre laser with variable power output up to 400W, and a laser track width of 150µm. To optimise the process parameters in order to achieve defect-free builds, the process parameters (laser power, scan speed, and scan spacing) were varied in the range of 50-120 W, 100-300 mm/s, and 45-150 µm, using a layer thickness of 20 µm, deposited using the M2 system island scanning strategy, with an island size of 5 mm, with a total of 30 build conditions. Following the optimisation to reduce the structural defects, the NPR structures were built using the optimum parameters.

### **2.2. Microstructural Characterisation and Mechanical Testing**

The as-fabricated (AF) samples were sectioned along the build (*z*) direction to study the influence of the process parameters on the pore and cracking density. The microstructure of the samples was analysed using a ZEISS Axioskop 2 optical microscope, and in a JOEL 6060 Scanning Electron Microscope (SEM), equipped with an Oxford Inca Energy-Dispersive X-ray Spectroscopy (EDX) system. To observe the microstructure at the interface between the various phases, thin foils were cut using spark erosion, ground, twin-jet electropolished in 5% perchloric acid in methanol solution, and examined using a JEOL2100 transmission electron

microscope (TEM), operated at 200 kV, and equipped with Oxford Inca EDX. The phases present at room temperature were identified using a Philips X'Per X-ray Diffraction (XRD) system, equipped with a Cu K $\alpha$  anode, operated at 35 kV. A Mettler-Toledo DSC1 Differential Scanning Calorimetry (DSC) system was used to determine the TTs, by cycling the samples at a rate of 10 °C/min during heating and cooling, between -10 and 130 °C.

Samples were also exposed to two different homogenisation treatments (HT1: 950°C/3h and HT2: 1000°C/2h, both followed by water quench). Their microstructure was also studied, and their TTs were characterised using DSC. Finally, the NPR structures in both the AF and HT2 conditions were compression tested at room temperature using a Zwick/Roell 1484 universal testing machine to measure the compressive properties and Poisson's ratio. Lubrication grease was applied on the contact surface between samples and machine to reduce radial friction. A 50 N preload was applied before testing. The displacement rate during compression test was 1 mm/min. Vertical displacement during compression test was recorded by the machine displacement and the horizontal displacement was measured during loading.

### 3. Results and Discussions

#### 3.1 Simulation and Design

Several types of geometries that produce NPR response have been studied and tested. Previous reports described the mechanical behaviour of re-entrant, chiral, and rotating NPR structures, with the re-entrant structures being the most studied. The unit cell of the re-entrant structure deforms its cell links in a way to exhibit a NPR on the level of each unit, which results in the highest NPR among the other types <sup>[1, 46]</sup>, and is hence the scope of this study. It is important to note that despite the isotropic properties of chiral and rotating structures, their deformation mechanism limits the NPR to be in the range of  $<-1$  <sup>[20-22]</sup>.

Two types of re-entrant structures were employed in this study; a conventional and a modified design, Error! Reference source not found.. As shown in (a), the conventional unit cell exhibits overhanging links, which are undesirable in AM processes. Overhanging links are generally described as critical structures to build by SLM, as they link onto loose powder, resulting in poor underside surfaces and resolution. Accordingly, the conventional design has been modified to overcome this problem by replacing all the overhangs structure with inclined ones as shown in (b).

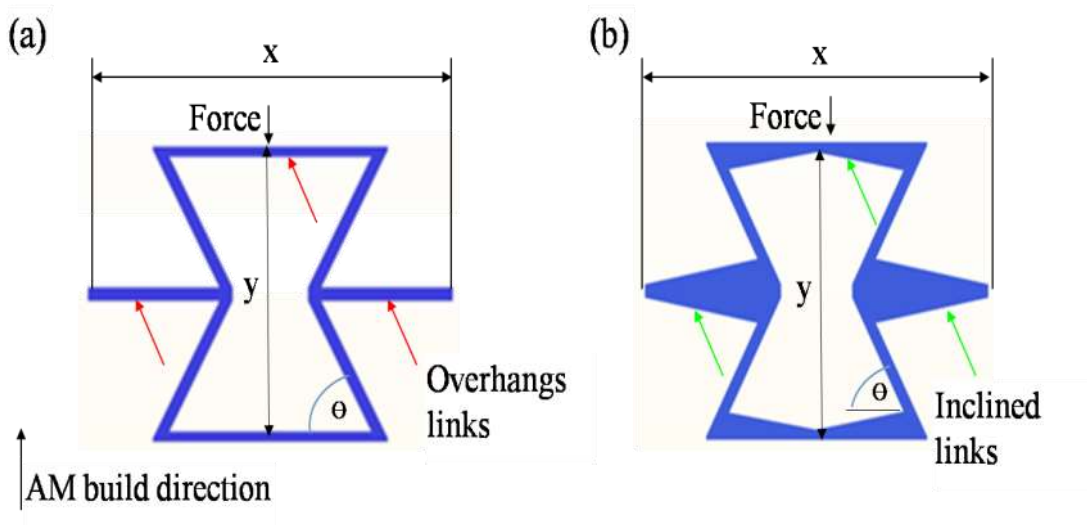


Figure 1: Re-entrant NPR unit cells (a) conventional unit cell, (b) Modified AM unit cell

Finite element analysis (FEA) using solidworks was used to predict the mechanical behaviour of the developed NPR structures. The area of the NPR structure was meshed using 8-node quadrilateral elements. The boundary conditions were set as follows: a compressive force was applied to top edges test while the bottom edges were fixed in the vertical (loading direction) and was allowed to move in the horizontal direction with friction coefficient of 0.2 to simulate a compression test. The effect of the re-entrant angle ( $\theta$ ) was calculated for both designs. The struts were made in 2D to reduce the meshing. The theoretical Poisson's Ratio ( $\nu$ ) values were calculated by dividing obtained FEA strain in the transverse direction ( $\epsilon_{\text{transverse}}$ ) to the strain in the vertical dimensions ( $\epsilon_{\text{vertical}}$ ), as shown in equation 1.

$$\nu = - \frac{\epsilon_{\text{transverse}}}{\epsilon_{\text{vertical}}} \quad (1)$$

Re-entrant angles ( $\theta$ ) were varied and the structures Poisson's ratios were calculated using FEA for the two designs shown in **Error! Reference source not found.** when subjected to compressive loading. **Error! Reference source not found.-a** shows the effect of the re-entrant angle on the calculated Poisson's ratio. As shown, the predicted Poisson's ratio increased as the re-entrant angle was increased for both designs. However, the conventional configuration with a re-entrant angle of  $75^\circ$  showed a Poisson's ratio of -1.88, slightly higher than the AM modified design, which showed a Poisson's ratio of -1.74. A 3D model was created based on the modified design using the optimum re-entrant angle for SLM fabrication and compression testing, as shown in **Error! Reference source not found.-b**. Similarly, for the 3D model, the calculated Poisson's ratio of the modified design showed a negative Poisson's ratio of -1.65.

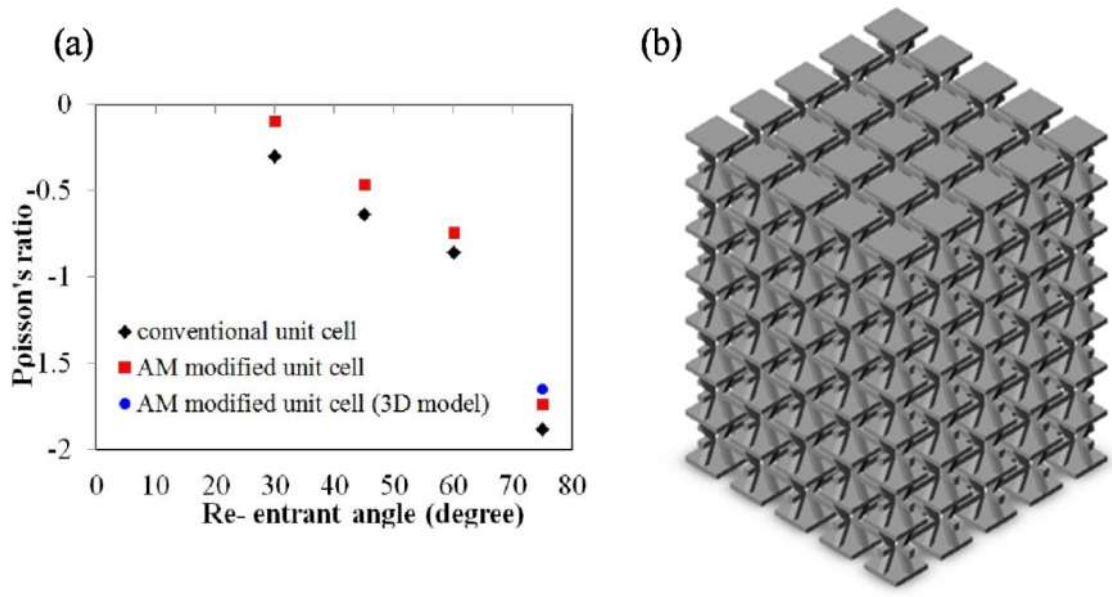


Figure 2: The design of the NPR structure (a) Effect of re-entrant angle on Poisson's ratio, (b) 3D construction of AM modified re-entrant design

### 3.2 Microstructural assessment of the powder and of SLMed samples

The as-received powder was generally spherical in shape (Figure 3-a), with limited satellites or irregular morphologies. This suggested a good flowability, which was evident in the measured Hausner ratio of 1.12 (good flowability < 1.25). By sectioning the powder particles, entrapped gas pores (due to atomisation) were infrequently observed (Error! Reference source not found.-b), suggesting that the powder quality is generally suitable for SLM since it is known that the presence of entrapped gas pores contributes to the residual porosity present in AM builds <sup>[47]</sup>. Powder size distribution showed that the average particle size ( $d_{50}$ ) is  $\sim 22\mu\text{m}$ , with a limited fraction in the sub-10  $\mu\text{m}$  range (Error! Reference source not found.-c). It was also noted that, despite the rapid cooling rates during gas atomisation, that  $\text{Ti}_2\text{Ni}$  intermetallics formed within the martensitic interdendritic regions in the powder particles (Error! Reference source not found.-b), which highlights the high susceptibility of this alloy to micro-segregation. According to the Ti-Ni phase diagram <sup>[43]</sup>, the alloy's composition

shows two phases at room temperature, which are the cubic  $Ti_2Ni$  and the monoclinic  $B19'TiNi$  [48].

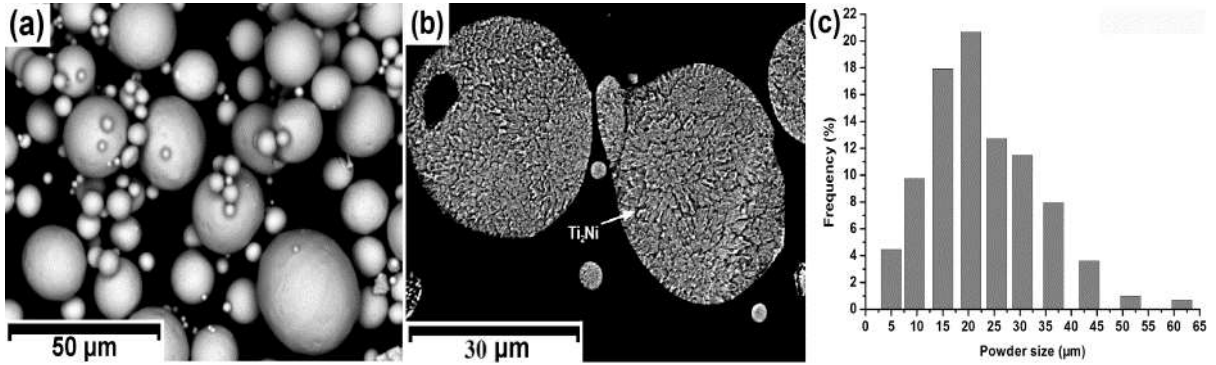


Figure 3: Re-entrant NPR unit cells (a) conventional unit cell, (b) Modified AM unit cell

### 3.3 Process Optimisation

Previous studies by Bormann and co-workers [38, 41] correlated the volumetric energy density parameter with the TTs in Ni-rich TiNi, whereby:

$$E_v = \frac{P}{v \times h \times t} \quad (2)$$

where  $E_v$  is energy density ( $J/mm^3$ ),  $v$  is scan speed (mm/s),  $h$  is scan spacing (mm), and  $t$  is layer thickness (mm). No studies in the literature used the energy density parameter to control the development of porosity content or cracking density in TiNi, although its use is a standard approach in other alloys [31, 49]. Typically, the porosity content is observed to decrease with the increase in the  $E_v$  until a threshold level is achieved indicating full consolidation [50]. However, this trend is absent in some alloy systems (e.g. Al-alloys) [51]. By plotting  $E_v$  versus the measured porosity area fraction, no trend was observed, with the data points showing a large scatter, **Figure 4**.

It is important to note that the investigated  $E_v$  range exceeded the range investigated in previous studies on Ni-rich TiNi [40]. It is also worth mentioning that the samples processed at

$E_V < 300 \text{ J/mm}^3$  demonstrated excessive cracking and lack of consolidation, **Error! Reference source not found.**, whereas the majority of the builds beyond  $300 \text{ J/mm}^3$  achieved porosity fraction  $< 1\%$ , yet with cracks present in some conditions.

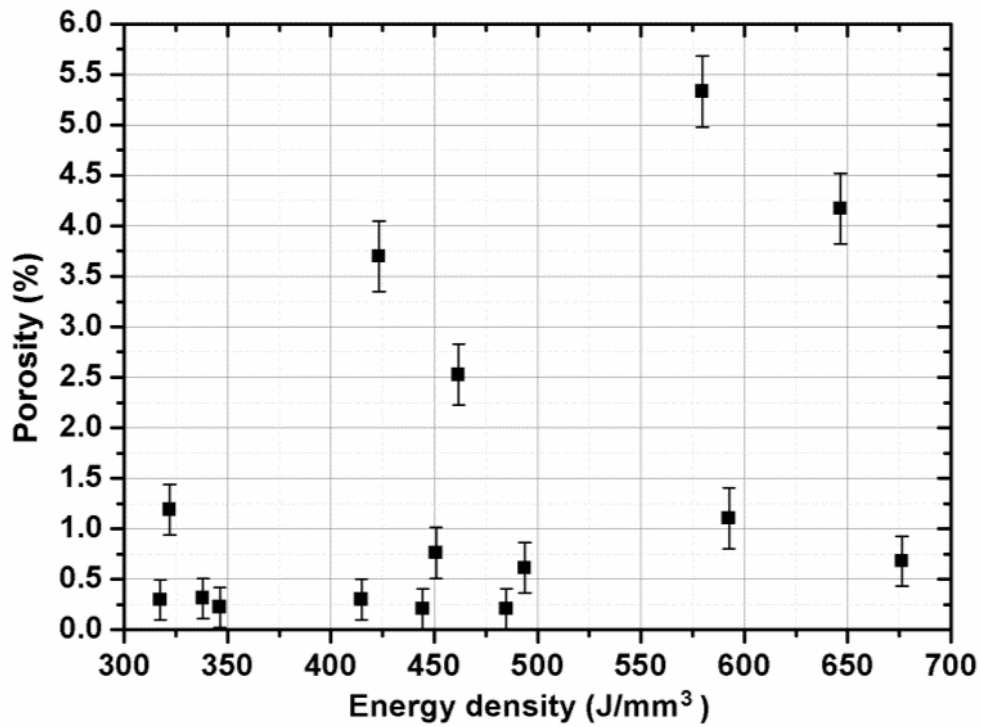


Figure 4: The energy density (EV) plot, showing the variation in porosity fraction in TiNi SLM

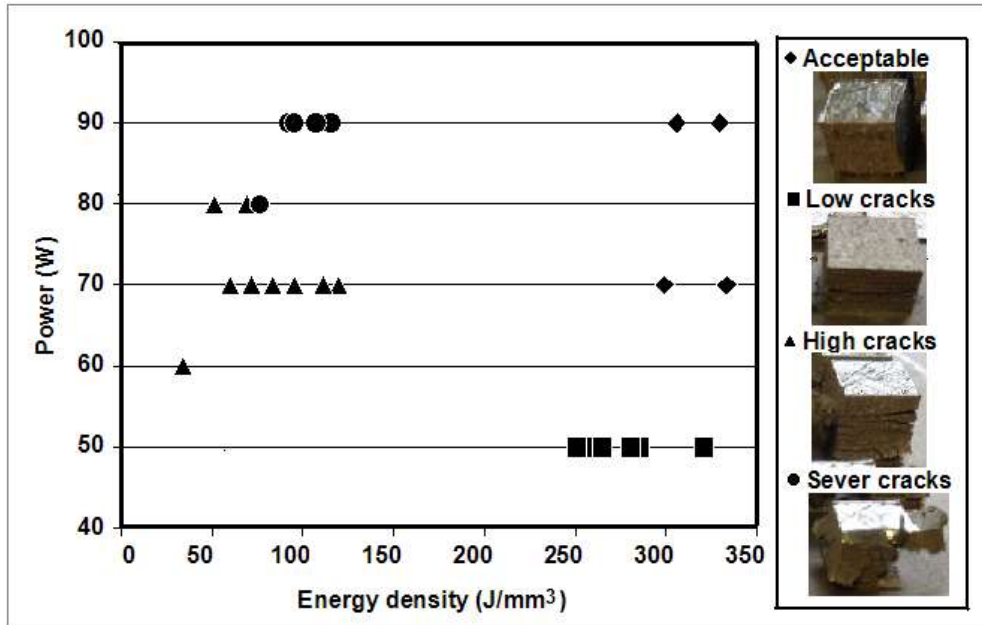


Figure 5: Lack of structural integrity in the samples built using  $EV < 350 \text{ J/mm}^3$

Alternative to  $E_V$ , the porosity fraction and cracking density (crack length/area,  $\text{mm/mm}^2$ ) were plotted against the linear energy density ( $E_L = P/v$ ,  $\text{J/mm}$ ), Figure 6-(a,b). Contour plots were constructed, showing the variation in the porosity fraction and cracking density as a function of both the scan spacing and  $E_L$ . By correlating both contours, processing windows to achieve low porosity fraction and low cracking density were identified, albeit separately in most conditions, since each defect type appeared to get reduced at a different parameters range. By choosing  $P/v = 0.67 \text{ J/mm}$  and scan spacing =  $0.065 \text{ mm}$ , a good compromise can be obtained in terms of the cracking density and porosity fraction. Still, a very narrow processing range showed low levels of both the porosity fraction and cracking density, as shown in **Error! Reference source not found.**-(c,d,e). Since lattice and mesh structures (including auxetics) typically have thin struts of diameter  $< 3 \text{ mm}$ , thermal cracks are known to be lower in those structures than in cubic/bulk specimens due to the differences in the level of thermal stresses experienced [45]. An interesting correlation can be inferred from **Error! Reference source not found.** It is obvious that low porosity can be achieved via a

combination of low  $E_L$  (**Error! Reference source not found.-a**), whereas low cracking density is obtained at high  $E_L$  (**Error! Reference source not found.-b**). This suggests that the cracking density tends to be reduced as the melt pool temperature increases (assuming that the melt pool temperature is proportional to  $E_L$ ). Evidence on the possibility of this hypothesis is the observation that high  $E_L$  resulted in high porosity fraction, since high melt pool temperatures are known to result in turbulences in the melt pool <sup>[47]</sup>.

### 3.4. Build Microstructure

The build microstructure exhibited three features; residual pores, cracks, and a dendritic solidification microstructure. The size of the pores in the high  $E_L$  samples varied between 10 to 60  $\mu\text{m}$ , **Figure 7-a**. Since the pores were generally large, spherical, and did not show unconsolidated particles within, it is believed that they were formed as a result of melt pool turbulences leading to gas entrapment, rather than from the porosity within the powder. The lowest porosity in the investigated parameters range was 0.09%, which is lowest ever found in studies on AM of TiNi, although the solidification behaviour (including porosity formation and susceptibility to macro and micro-cracking) would be expected to be alloy-dependent <sup>29,30,33</sup>, so it may be higher in other alloys. The microstructure was primarily dendritic, with  $\text{Ti}_2\text{Ni}$  present along the interdendritic regions. The dendritic structure was finer in the low  $E_L$  conditions (e.g. **Figure 7-(b,c)**), compared to the high  $E_L$  conditions (**Figure 7-a**), which suggests that slower cooling rates occurred in the high  $E_L$  conditions. The high  $E_L$  condition consisted of 20-60  $\mu\text{m}$  columnar and 5-10  $\mu\text{m}$  equiaxed dendrites **Figure 7-a**), compared to fine columnar dendrites of 10-40  $\mu\text{m}$  in length in low  $E_L$  condition (**Figure 7-b**). The  $\text{Ti}_2\text{Ni}$  content was quantified using ImageJ<sup>®</sup> image analysis, revealing an area fraction of  $31\pm 4\%$  ( $18\pm 4$  vol.%) in the high  $E_L$  condition (90 W, 115 mm/s, 0.0675 mm), compared to  $27\pm 4\%$  ( $14\pm 4$  vol.%) in the low  $E_L$  condition (60 W, 120 mm/s, 0.056 mm).

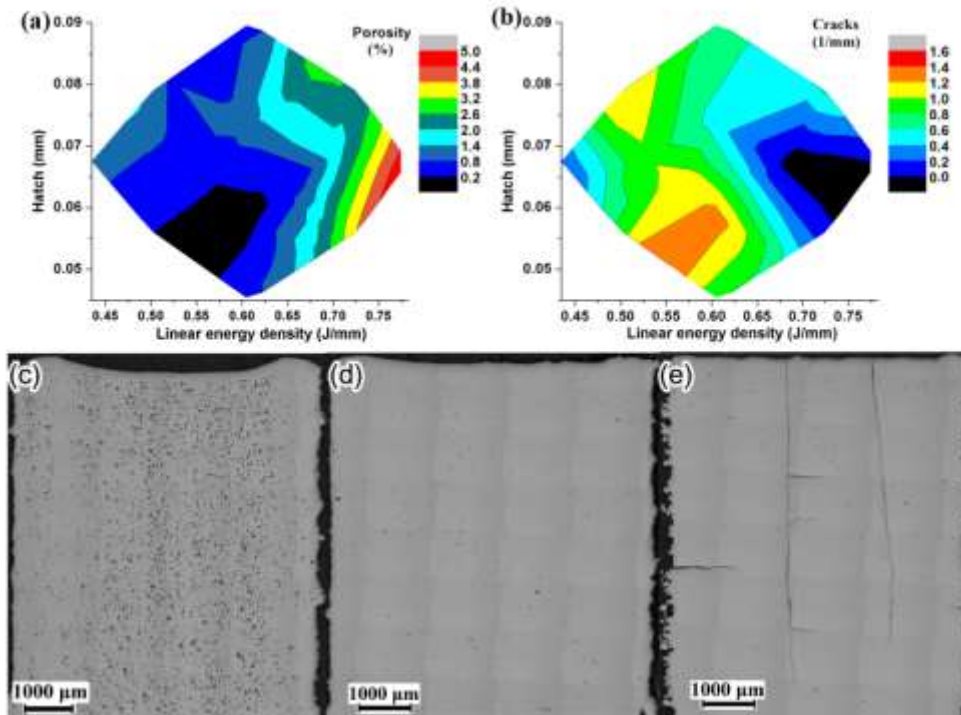


Figure 6: The correlation of the EL and cracking density with the (a) porosity fraction and (b) crack density, showing representative builds from the extremes of the investigated window; (c) low cracking only (90 W, 115 mm/s, 0.0675 mm, high EL), (d) low cracking and low porosity (70W, 105 mm/s, 0.0675 mm), and (e) low porosity with long cracks (60 W, 120 mm/s, 0.056 mm, low EL).

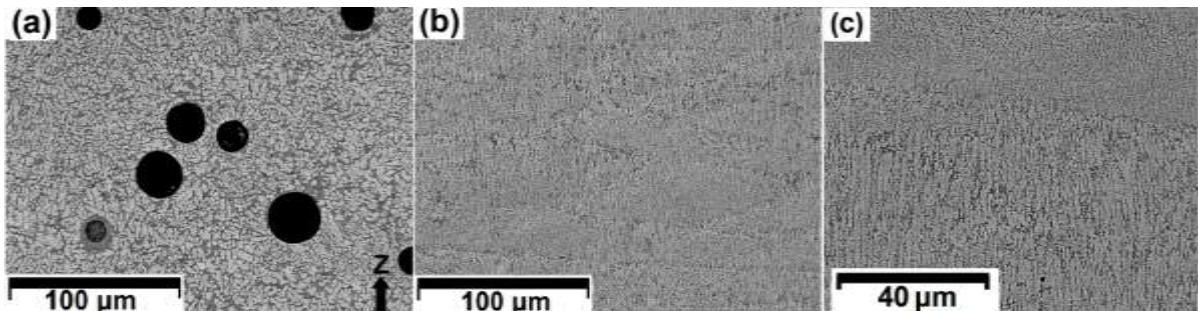


Figure 7: The morphology of the horizontal thermal cracks (arrowed) at the edge of near full-density sample and the vertical cracks that appeared after sectioning, shown in (a) optical micrograph showing cracks initiating from interdendritic  $Ti_2Ni$  in (b) and (c) back-scatter micrographs of X-Z section showing the frequency of the cracks

The high  $Ti_2Ni$  content suggests that a heat treatment is necessary to improve the homogeneity, mechanical properties, and shape memory behaviour of SLM-built SMA. Since  $Ti_2Ni$  is very brittle, cracks appeared to stem from the continuous  $Ti_2Ni$  phase present in the

interdendritic regions, Error! Reference source not found.-(a,b). As a result, it is believed that the ductility of the as-built samples is going to be poor due to the propagation and growth of the existing micro-cracks. The majority of the macro-cracks cracks were horizontal (i.e. normal to the build direction), Figure 8-c. Although the critical stress of TiNi is rather low (about 300MPa in the martensite phase and about 400 MPa in the austenite phase), the strain can be higher than 20% during tensile tests <sup>[52]</sup>. The vertical cracks appeared to form only after sectioning, and presumably occur as a mechanism to relax the residual stresses. Despite the high porosity fraction present in the high  $E_L$  conditions, this coincides with low cracking density, suggesting that the presence of porosity allows more deformation within the samples, which potentially reduces the cracking density, (Error! Reference source not found.-b). Mechanical testing of porous TiNi structures also supports this hypothesis <sup>[53, 54]</sup>.

XRD result of the powder and as-fabricated samples (built using the low  $E_L$  and high  $E_L$  parameters) confirmed the presence of two phases only;  $Ti_2Ni$  and B19', Figure 9. The data indicate that the as-fabricated samples of various build conditions have similar peaks, but the peaks intensities are different, while the powder has random orientations.

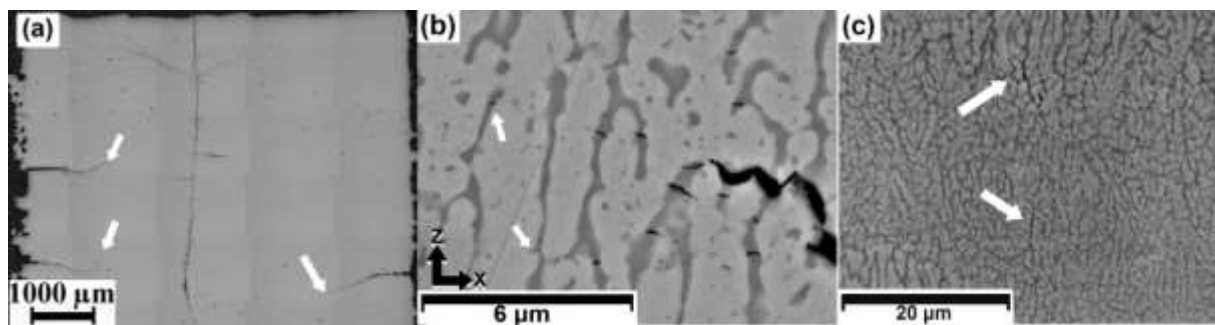


Figure 8: The morphology of the horizontal thermal cracks (arrowed) at the edge of near full-density sample and the vertical cracks that appeared after sectioning, shown in (a) optical micrograph showing cracks initiating from interdendritic  $Ti_2Ni$  in (b) and (c) back-scatter micrographs of X-Z section showing the frequency of the cracks

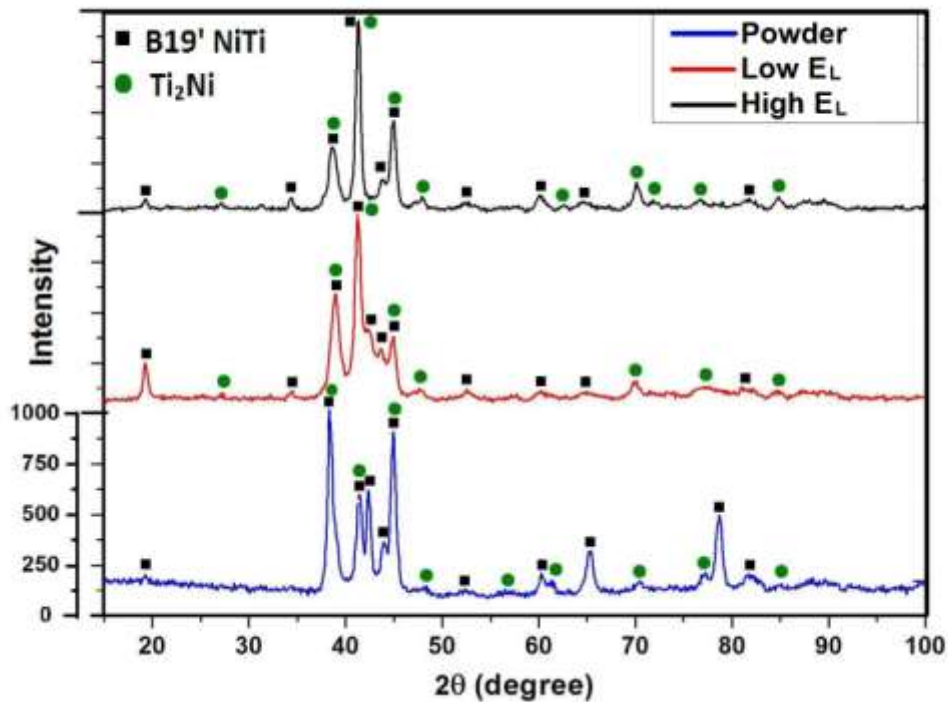


Figure 9: XRD patterns for SLM built TiNi and powders reveal the presence of B19' and Ti<sub>2</sub>Ni. The high EL sample has larger amount of Ti<sub>2</sub>Ni than the low EL sample, while the powder (blue) has random orientations

### 3.5. Post SLM Heat Treatments

The presence of Ti<sub>2</sub>Ni intermetallics disturbs the chemistry of the matrix by depleting the matrix from Ti, resulting in a drop in the TTs. Furthermore, large amounts of Ti<sub>2</sub>Ni may negatively affect the SMA ductility. As a result, a heat treatment is essential to improve the homogeneity, SME, and mechanical properties. According to the TiNi binary phase diagram, Ti<sub>2</sub>Ni phase melts at 964°C. However, this temperature can be affected by the presence of O and other minor elements. As such, DSC was used to accurately determine the melting temperature of Ti<sub>2</sub>Ni. The DSC revealed that Ti<sub>2</sub>Ni melting initiates at ~1010°C, **Error!**  
**Reference source not found..**

Thus, two heat treatments (HT1 and HT2) were applied to the optimum build condition. HT2 is close to the melting point of Ti<sub>2</sub>Ni in this alloy, which was intended to potentially

consolidate the micro-cracks in  $Ti_2Ni$  by melting and re-solidification. HT1 appeared to break most of  $Ti_2Ni$  (Error! Reference source not found.-a, whereas HT2 eliminated the continuous  $Ti_2Ni$  interdendritic morphology altogether (Error! Reference source not found.-b).

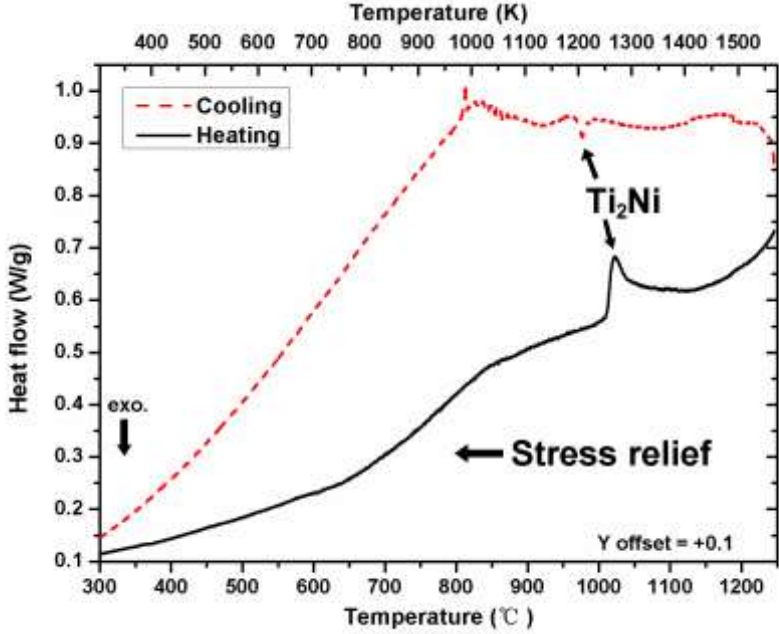


Figure 10: DSC trace of the low EL AF condition shows  $Ti_2Ni$  melts  $\sim 1010^\circ C$  and solidified about  $980^\circ C$  during cooling

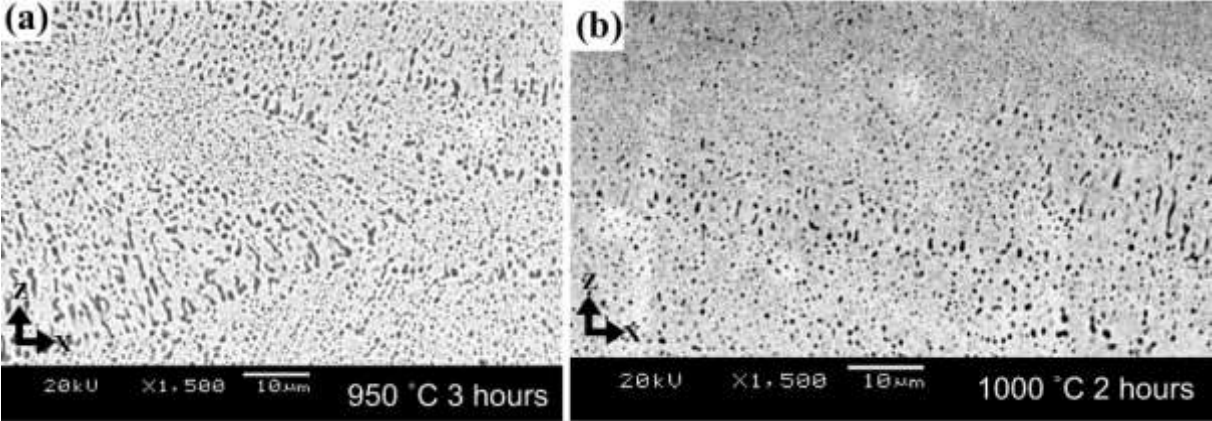


Figure 11: The morphology of  $Ti-2-Ni$  phase following the post-process homogenisation heat treatments (a) HT1, (b) HT2.

**3.6. The Phase Transformation Behaviour**

The phase transformation behaviour and TTs of the builds were studied using DSC in the as-fabricated and HT2 conditions. Initially, the samples were thermally cycled in their

transformation range to stabilise their behaviour <sup>[43, 55]</sup>, before recording the DSC traces, **Error! Reference source not found.** It appears that the heat treatment resulted in an increase in the TTs, due to dissolution of the excess Ti<sub>2</sub>Ni formed during the process, which increased the Ti at.% content within the B19', leading to an increase in the martensite start temperature (M<sub>s</sub>). Only one-step transformation was observed.

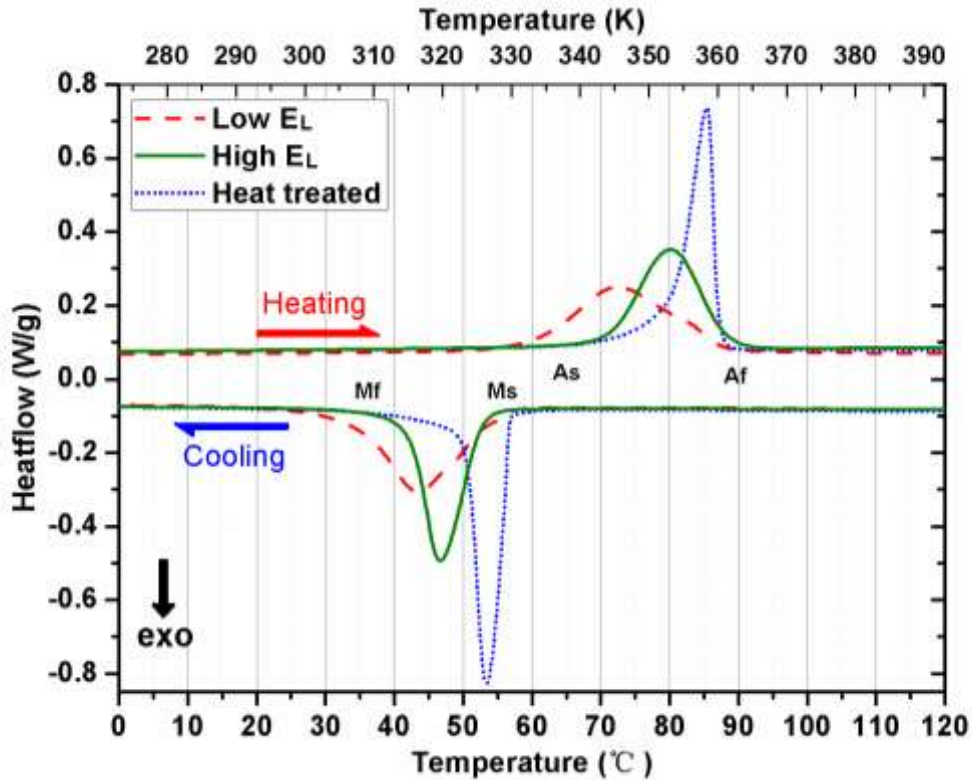


Figure 12: DSC traces for the as-built low E<sub>L</sub> and high E<sub>L</sub> and heat-treated low E<sub>L</sub> samples

By calculating the energy release during the martensitic transformation, it was found to be 19.5 J/g for the low E<sub>L</sub> condition, 17.9 J/g for the high E<sub>L</sub> build (~10% lower than low E<sub>L</sub> sample), and 19.3 J/g for the HT2 low E<sub>L</sub> condition. The change in the energy release can be correlated to the fraction of B19' present in the sample. As such, this suggests that the low E<sub>L</sub> condition and the heat-treated condition generally contain more B19' fraction (and lower Ti<sub>2</sub>Ni fraction) than in the high E<sub>L</sub> condition, which can be verified from **Figure 7-(a,b)**. The

Ti<sub>2</sub>Ni fraction ( $P_{\text{Ti}_2\text{Ni}}$ ) was also estimated using the integrated intensity of the XRD patterns (**Figure 9**) using the equation:

$$P_{\text{Ti}_2\text{Ni}} = \frac{\sum C_j}{\sum C_i} \quad (3)$$

where  $C_j$  is the integrated intensity of Ti<sub>2</sub>Ni peak and  $C_i$  are the peak intensity for all phases, it was found that the total intensity of Ti<sub>2</sub>Ni in the high  $E_L$  sample is 33±2%, which is about 10% higher than the low  $E_L$  sample (23±2%), which confirms the previous hypothesis.

The heat treatment also led to a narrower phase transformation range (i.e.  $M_s - M_f$ ). The narrowness of the peak in the heat-treated sample shows that the heat treatment has homogenised the samples, eliminating chemical segregation within the B19' <sup>[56]</sup>. The low  $E_L$  sample has the widest martensitic transformation peak, ranging from 56 to 22°C, whereas the high  $E_L$  sample has a narrower martensitic peak, while the heat-treated sample has the narrowest peak, **Error! Reference source not found.** The peak width is related the inhomogeneity of the B19' matrix. If the B19' shows chemical inhomogeneities in the Ti-content, it is possible that the TTs range will end up being extended over a wider area. The energy release, however, is related to the B19' fraction. As a result, the heat-treated sample has the most homogeneous B19' chemistry, which results in the narrowest TTs range. Using the TEM, some Ni-rich areas were found in the TiNi matrix in the low  $E_L$  sample. As shown in **Figure 13**, the Ti-rich or near equiatomic matrix with twinned martensite are indicated by black arrow. The area near Ti<sub>2</sub>Ni indicated by the white arrow showed 51 at.% Ni using EDX, which happens to be at the vicinity of some Ti<sub>2</sub>Ni particles. This could explain the wider martensitic TTs range in the low  $E_L$  condition (**Error! Reference source not found.**). It also suggests that chemical inhomogeneities have a strong influence on the SME, and as such a post-process heat treatment is essential to improve the performance.

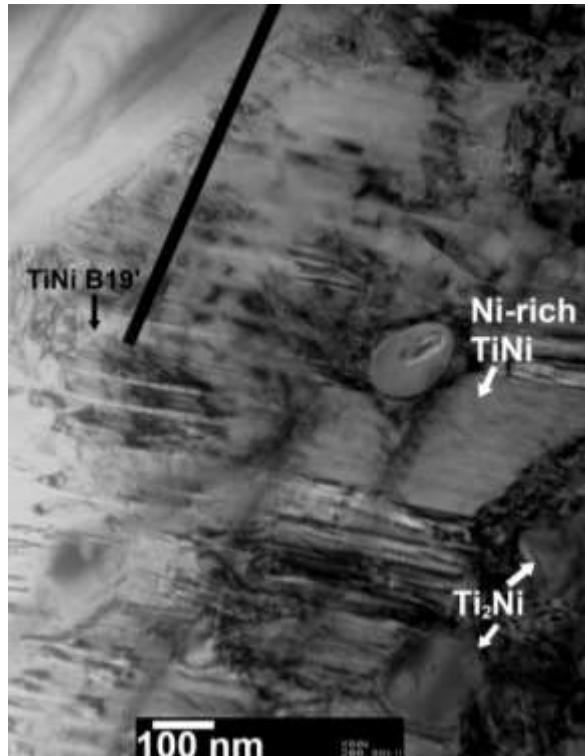


Figure 13: Darkfield TEM micrograph of low EL sample, the presence of Ni-rich B19' (indicated by the black arrow) at the vicinity of Ti<sub>2</sub>Ni particles. The EDX analysis of the martensite area indicated by the black arrow was 51 at.% Ti, while the Ni-rich area at the vicinity of Ti<sub>2</sub>Ni indicated by white arrow was Ni-rich (49 at.% Ti).

### 3.8. NPR Structure Morphology and Performance

Conventional re-entrant structure (**Error! Reference source not found.**-a) samples with dimensions  $(x,y,z)$  of  $26 \times 26 \times 36 \text{ mm}^3$  were built using the low  $E_L$  parameters. The designed beam thickness was 0.3 mm, while the beam thickness in the fabricated samples was found to be  $\sim 1\text{-}2 \text{ mm}$ , 0.8 mm powder lumps attached at the corners. This is a known shortcoming in SLM, where the thermal footprint of the laser is usually large than the optical footprint (laser spot size), which is usually the one accounted for in the calculation of the tool path. As a result, the melt pool ends up consolidating (partially or fully) some of the powder particles at its vicinity in the bed. Furthermore, there are obvious locations where the thickness of the struts changes (e.g. comparing the corners with the struts). This happens due to the delivery of more heat input in the location where there is a crossover of the laser tracks. Finally, the amount of solid/fabricated metal at the corner is less than the other area, which leads

variations of heat transferring rate. It can be clearly see the poor underside surfaces due to the overhangs structures of the conventional design. These defects were minimised in the modified AM re-entrant structure, **Error! Reference source not found.**-b. As expected, the microstructure of the struts does not show any cracks in the optimised condition, due to the rapid cooling experienced in the small sections, **Error! Reference source not found.**-c.

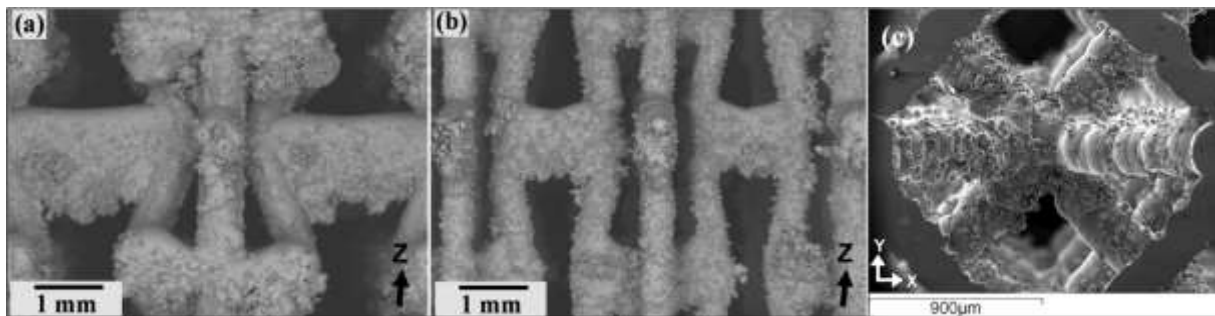


Figure 14: The morphology of NPR cells showing SEM micrographs for the (a) conventional re-entrant design, (b) modified AM re-entrant design, and (c) a section through the struts showing the lack of cracks

Mechanical tests were carried on before and after HT2 to assess the influence of the heat treatment on the mechanical performance. The force-displacement curves for the as-fabricated and heat-treated samples are shown in **Error! Reference source not found.** The as-fabricated sample shows a steeper force/displacement curve than the heat-treated sample, and the maximum load is 12% higher than the heat-treated sample. The as-fabricated sample also shows a generally linear curve prior to fracture, whereas the heat-treated sample shows two steps deformation. However, the extent of deformation in the as-fabricated sample was 46% lower than the heat-treated sample, which indicates the ductility improved after the heat treatment. The as-fabricated sample includes more  $Ti_2Ni$ , which increases the yield strength due to its strengthening contribution <sup>[52, 57]</sup>. However, the surface features make susceptible to stress concentration and crack propagation along the interdendritic  $Ti_2Ni$ , which reduce the ductility of as-fabricated sample. The dissolution of  $Ti_2Ni$  in the heat-treated samples, however, allows the material to have a large deformation prior to failure.

Force–displacement data were used to calculate Poisson’s ratio using Equation 1. The Poisson’s ratio of the heat-treated NPR structure is  $\sim -2$ , which is similar to the Ti-6Al-4V NPR structure fabricated by electric beam melting, previously reported in the literature [21]. Following deformation, the deformed structure was heated to 100°C, which led to the restoration of the original (undeformed) geometry.

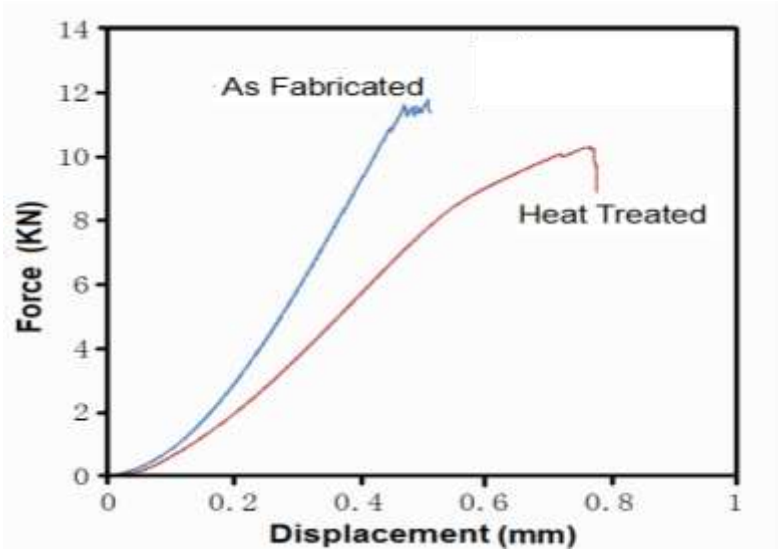


Figure 15: Force-displacement curve shows the as-fabricated sample (blue) has higher strength but lower ductility than the heat-treated sample (red).

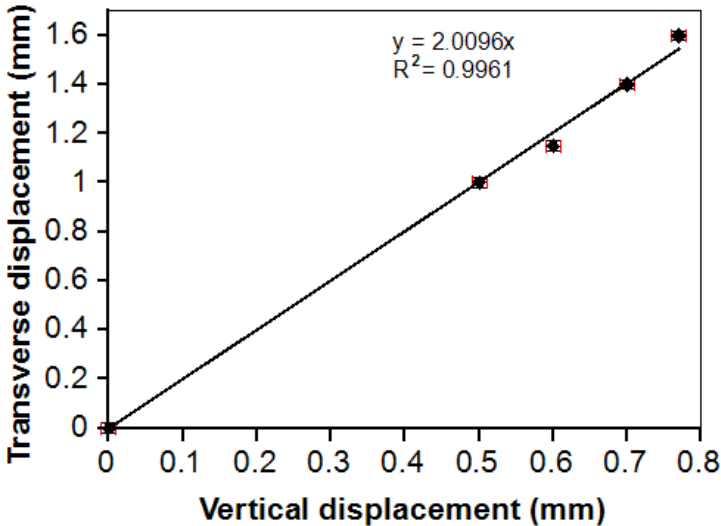


Figure 16: The Poisson’s ratio  $\nu_{tz}$  (-2) was calculated as the negative ratio between the transverse and vertical deformation from the best fit of force-displacement data of heat treated sample

#### **4. Conclusions and Future Work**

The study focused on the development of TiNi-based NPR structures using AM. The key findings of this work can be summarised as follows:

1. Design optimisation of NPR structures is essential to tailor the Poisson's ratio and to adapt the structure for AM by avoiding the use of overhanging structures.
2. SLM of TiNi demonstrates two potential defects; porosity and residual stress induced cracking. Both types can be minimised or totally eliminated through process optimisation. The use of the linear energy density proved to be a useful tool in identifying the process window for SLM of TiNi.
3. Heat treatment is essential to improve the microstructural homogeneity, SME, and ductility of TiNi, through the reduction of Ti<sub>2</sub>Ni precipitates. Nonetheless, the reduction in Ti<sub>2</sub>Ni results in a reduction in load bearing capability of the structure.
4. The heat-treated NPR structure achieved a high negative Poisson's ratio of -2.

Future work will focus the stability of the SME in NPR structure with repeated loading and unloading.

#### **Acknowledgements**

KE and MA would like to acknowledge the support from the Centre of Defence Enterprise (CDE) and the Defence Science and Technology Laboratory (Dstl) (grant # CDE31263). MA and NJA would like to also acknowledge the support received from FP7 AMAZE programme that allowed the continuation of this work.

## References

- [1] Dong L, Liang D, Lakes RS. The properties of copper foams with negative Poisson's ratio via resonant ultrasound spectroscopy. *Physica Status Solidi B - Basic Solid State Physics* 2013;250:1983-7.
- [2] Valant M, Axelsson AK, Aguesse F, Alford NM. Molecular Auxetic Behavior of Epitaxial Co-ferrite Spinel Thin Film. *Advanced Functional Materials* 2010;20:644-7.
- [3] Gupta N, Gupta KM. Metamaterial and auxetic hybrid composite antennas. 2005 IEEE International Workshop on Antenna Technology: Small Antennas and Novel Metamaterials, 7-9 March 2005. Piscataway, NJ, USA: IEEE; 2005. p. 414-17.
- [4] Junghyuk K, Bhullar S, Yonghyun C, Lee PC, Jun MBG. Design and fabrication of auxetic stretchable force sensor for hand rehabilitation. *Smart Materials and Structures* 2015;24:075027 (8 pp.).
- [5] Zhengyue W, Hong H, Xueliang X. Deformation behaviors of three-dimensional auxetic spacer fabrics. *Textile Research Journal* 2014;84:1361-72.
- [6] Diaz Lantada A, Muslija A, Garcia-Ruiz JP. Auxetic tissue engineering scaffolds with nanometric features and resonances in the megahertz range. *Smart Materials and Structures* 2015;24:055013 (14 pp.).
- [7] Mousanezhad D, Ebrahimi H, Haghpanah B, Ghosh R, Ajdari A, Hamouda AMS, et al. Spiderweb honeycombs. *International Journal of Solids and Structures* 2015;66:218-27.
- [8] Qiao JX, Chen CQ. Impact resistance of uniform and functionally graded auxetic double arrowhead honeycombs. *International Journal of Impact Engineering* 2015;83:47-58.
- [9] Yang L, Harrysson O, West H, Cormier D. Mechanical properties of 3D re-entrant honeycomb auxetic structures realized via additive manufacturing. 2015.
- [10] Bacigalupo A, De Bellis ML. Auxetic anti-tetrachiral materials: Equivalent elastic properties and frequency band-gaps. *Composite Structures* 2015;131:530-44.
- [11] Zied K, Al-Grafi M. Design of auxetic sandwich panel faceplates comprising cellular networks with high stiffness and negative Poissons ratio. 2015.
- [12] Webber RS, Alderson KL, Evans KE. Novel variations in the microstructure of the auxetic microporous ultra-high molecular weight polyethylene. 1. Processing and microstructure. *Polymer Engineering and Science* 2000;40:1894-905.
- [13] Alderson A, Evans KE. Microstructural modelling of auxetic microporous polymers. *Journal of Materials Science* 1995;30:3319-32.
- [14] Alderson A, Evans KE. Modelling concurrent deformation mechanisms in auxetic microporous polymers. *Journal of Materials Science* 1997;32:2797-809.
- [15] Grima JN, Cauchi R, Gatt R, Attard D. Honeycomb composites with auxetic out-of-plane characteristics. *Composite Structures* 2013;106:150-9.
- [16] Jayanty S, Crowe J, Berhan L. Auxetic fibre networks and their composites. *Physica Status Solidi B* 2011;248:73-81.
- [17] Subramani P, Rana S, Oliveira DV, Fangueiro R, Xavier J. Development of novel auxetic structures based on braided composites. *Materials & Design* 2014;61:286-95.
- [18] Glazzard M, Breedon P. Weft-knitted auxetic textile design. *Physica Status Solidi B - Basic Solid State Physics* 2014;251:267-72.
- [19] Zhengyue W, Hong H. Auxetic materials and their potential applications in textiles. *Textile Research Journal* 2014;84:1600-11.
- [20] Elipe J, Lantada A. Comparative study of auxetic geometries by means of computer-aided design and engineering. *Smart Materials and Structures* 2013;21: 105004.
- [21] Schwerdtfeger J, Heintl P, Singer RF, Körner C. Auxetic cellular structures through selective electron-beam melting. *physica status solidi (b)* 2010;247:269-72.
- [22] Yang L, Harrysson O, West H, Cormier D. Design and characterization of orthotropic re-entrant auxetic structures made via EBM using Ti6Al4V and pure copper. 22nd Annual

- International Solid Freeform Fabrication Symposium - An Additive Manufacturing Conference, SFF 2011, August 8, 2011 - August 10, 2011. Austin, TX, United states: University of Texas at Austin (freeform); 2011. p. 464-74.
- [23] Buenconsejo PJS, Zarnetta R, König D, Savan A, Thienhaus S, Ludwig A. A New Prototype Two-Phase (TiNi)-(β-W) SMA System with Tailorable Thermal Hysteresis. *Advanced Functional Materials* 2011;21:113-8.
- [24] Lagoudas DC. *Shape Memory Alloys: Modeling and Engineering Application*. Springer 2008.
- [25] Zhi Shan Yuan ZWF, Jiang Bo Wang, Wei Dong Miao, Chong Jian Li, Wei Liu The Segregation of Chemical Composition in NiTi Shape Memory Alloy Melted by VIM in Lime Crucible *Materials Science Forum* 2009;610-613:3.
- [26] GHOSH A. Segregation in cast products. *Sadhana* 2001;26:20.
- [27] K. WS, C. LH, C. CC. A study on the machinability of a Ti49.6Ni50.4 shape memory alloy. *Materials Letters* 1999;40:5.
- [28] D. S. Forming nitinol—a challenge. *New Developments in Forming Technology* 2001.
- [29] J. Frenzel ZZ, Ch. Somsen, K. Neuking, G. Eggeler. Influence of carbon on martensitic phase transformations in NiTi shape memory alloys. *Acta Materialia* 2007;55:10.
- [30] William J. Buehler FEW. A summary of recent research on Nitinol alloys and their potential application in ocean engineering. *Ocean Engineering* 1967;1:20.
- [31] Wu X. A Review of Laser Fabrication of Metallic Engineering Components and of Materials. *Materials Science and Technology* 2007;23:10.
- [32] Vayre B, Vignat F, Villeneuve F. Identification on some design key parameters for additive manufacturing: Application on Electron Beam Melting. 46th CIRP Conference on Manufacturing Systems, CIRP CMS 2013, May 29, 2013 - May 30, 2013. Setubal, Portugal: Elsevier; 2013. p. 264-9.
- [33] Zhang B, Chen J, Coddet C. Microstructure and Transformation Behavior of in-situ Shape Memory Alloys by Selective Laser Melting Ti–Ni Mixed Powder. *Journal of Materials Science & Technology* 2013;29:863-7.
- [34] Mohsen Taheri Andani NSM, Christoph Haberland, David Dean, Michael J. Miller, Mohammad Elahinia,. *Metals for bone implants. Part 1. Powder metallurgy and implant rendering. Acta Biomaterialia* 2014;10:12.
- [35] Xiong JY, Li YC, Wang XJ, Hodgson PD, Wen CE. Titanium–nickel shape memory alloy foams for bone tissue engineering. *Journal of the Mechanical behavior of Biomedical Materials* 2007;2008:5.
- [36] S. Shiva IAP, S.K. Mishra, C.P. Paul, L.M. Kukreja. Investigations on the influence of composition in the development of Ni-Ti shape memory alloy using laser based additive manufacturing. *Optics & Laser Technology* 2014;69:7.
- [37] I. Shishkovsky FM, I. Smurov. Direct Metal Deposition of Functional Graded Structures in Ti-Al System. *Physics Procedia* 2012;39:9.
- [38] Bormann T, Müller B, Schinhammer M, Kessler A, Thalmann P, Wild Md. Microstructure of selective laser melted nickel-titanium. *Materials Characterization* 2014;94:14.
- [39] Elahinia MH, Hashemi M, Tabesh M, Bhaduri SB. Manufacturing and processing of NiTi implants: A review. *Progress in Materials Science* 2012;57:911–46.
- [40] Dadbakhsh S, Speirs J M, Kruth e-P, Schrooten J, Luyten J, Humbeeck JV. Effect of SLM Parameters on Transformation Temperatures of Shape Memory Nickel Titanium Parts. *Advanced Engineering Materials* 2014;2014:7.
- [41] Bormann T, Schumacher R, Müller B, Mertmann M, Wild Md. Tailoring Selective Laser Melting Process Parameters for NiTi Implants. *Journal of Materials Engineering and Performance* 2012;21:6.
- [42] J.X. Zhang MS, A. Ishida. On the Ti<sub>2</sub>Ni precipitates and Guinier-Preston zones in Ti-rich

Ti-Ni thin films. *Acta Materialia* 2003;51:10.

[43] K. Otsuka XR. Physical metallurgy of Ti–Ni-based shape memory alloys. *Progress in Materials Science* 2005;50:168.

[44] Stavroulakis GE. Auxetic behaviour: appearance and engineering applications. *Physica status solidi (b)* 2005;242:10.

[45] Wang K, Chang Y-H, Chen Y, Zhang C, Wang B. Designable dual-material auxetic metamaterials using three-dimensional printing. *Materials and Design* 2014;67:6.

[46] Lakes R. Foam structures with a negative Poisson's ratio. *Science* 1987;235:1038-40.

[47] Grong O. *Metallurgical Modelling of Welding*. The Institute of Materials 1997;3.

[48] Z. Lekston EL. X-ray Diffraction Studies of NiTi Shape Memory Alloys. *Archives of Materials Science and Engineering* 2007;28:7.

[49] Thijs L, Verhaeghe F, Craeghs T, Humbeeck JV, Kruth J-P. A study of the microstructural evolution during selective laser melting of Ti–6Al–4V. *Acta Materialia* 2010;58:3303-12.

[50] F. Wang XHWaDC. On direct laser deposited Hastelloy X: dimension, surface finish, microstructure and mechanical properties. *Materials Science and Technology* 2011;27:13.

[51] E.O. Olakanmi RFC, K.W. Dalgarno Densification mechanism and microstructural evolution in selective laser sintering of Al-12Si powders. *Journal of Materials Processing Technology* 2010;211:8.

[52] Gall K, Sehitoglu H, Anderson R, Karaman I, Chumlyakov YI, Kireeva IV. On the mechanical behavior of single crystal NiTi shape memory alloys and related polycrystalline phenomenon. *Materials Science and Engineering A* 2001;317:8.

[53] Zhang XP, Liu HY, Yuan B, Zhang YP. Superelasticity decay of porous NiTi shape memory alloys under cyclic strain-controlled fatigue conditions. *Materials Science and Engineering A* 2007;481-482:4.

[54] N. Resnina SB, A. Voronkov, V. Mozgunov, A. Krivosheev, I. Ostapov. Martensitic transformation and mechanical behavior of porous Ti-50.0 at % Ni alloy, fabricated by self-propagating high temperature synthesis at different temperature. *Physics Procedia* 2010;10:6.

[55] W S Lai BXL. Lattice Stability of Some Ni-Ti Alloy Phases Versus Their Chemical Composition and Disorder. *Journal of Physic* 2000;12:8.

[56] K. Sadrezaad FM, and R.Sharghi. Heat treatment of Ni-Ti alloy for improvement of Shape Memory Effect. *Materials and Manufacturing Processes* 1997;12:9.

[57] Johnson WL. *Bulk Glass-Forming Metallic Alloys: Science and Technology*. MRS Bulletin 1999;24:14.

[58] Laser C. Hofmann, Hofmann Innovation Group Website. <<http://wwwhofmann-innovation.com/en/technologies/direct-cusing-manufacturinghtml>> 2012.

[59] Luke N. Carter CM, Philip J. Withers, Moataz M. Attallah. The influence of the laser scan strategy on grain structure and cracking behaviour in SLM powder-bed fabricated nickel superalloy. *Journal of Alloys and Compounds* 2014;615:9.